IEEE Access
Multidisciplinary ⋮ Rapid Review ⋮ Open Access Journal

Received 24 October 2022, accepted 8 November 2022, date of publication 10 November 2022, date of current version 18 November 2022.

Digital Object Identifier 10.1109/ACCESS.2022.3221461

RESEARCH ARTICLE

4-Pole Tunable Absorptive Bandstop Filters Using Folded Coupled-Lines With an Inductor

YOUNG-HO CHO[1], (Member, IEEE), CHEOLSOO PARK[2], (Member, IEEE), AND SANG-WON YUN[3], (Life Member, IEEE)

[1]Department of Electrical and Communication Engineering, Daelim University College, Anyang, Gyeonggi-do 13916, South Korea
[2]Computer Engineering Department, Kwangwoon University, Seoul 01897, South Korea
[3]Department of Electronics, Sogang University, Seoul 04107, South Korea

Corresponding author: Cheolsoo Park (parkcheolsoo@kw.ac.kr)

This work was supported by the National Research Foundation of Korea (NRF), Korea Government (MSIT), under Grant NRF-2017R1A5A1015596.

ABSTRACT The ever-growing field of wireless communication requires efficient radio frequency transceivers with tunable absorptive bandstop filters that can prevent the interference of out-of-band and reflected signals. This paper presents 4-pole tunable absorptive bandstop filters using folded coupled-lines with an inductor. A 4-pole filter transfer function is achieved to obtain an absorptive bandstop filter coupling diagram with 45° electrical-length transmission-line source/load coupling. The folded-loaded coupled-lines with an inductor are proposed to obtain the control for the required coupling coefficients based on the filter transfer functions. The required quality factor extracted through the transfer function is accomplished using a distributed resonator loaded with asymmetrical varactors without auxiliary circuits, such as an impedance-matching network. Two types of filters were designed and built on a substrate with $\varepsilon_r = 3.42$ and $h = 30$ mil. The center frequency tuning was performed using silicon varactors. The first filter shows a return loss of 16.2–38 dB and a rejection level of 41–48 dB in the tuning range 0.83–1.09 GHz. The second filter results in a measured return loss of 14–34 dB and a rejection level of 40.1–51 dB at 1.16–1.47 GHz. 4-pole tunable absorptive bandstop filters with high attenuation and reflectionless responses were achieved which have applications in cognitive radios and carrier aggregation systems.

INDEX TERMS Absorptive response, bandstop filter, folded coupled-line, tunable filter.

I. INTRODUCTION

Adaptive wireless communication systems have been developed to enable reliable communication under extreme radio frequency (RF) spectrum conditions. Tunable absorptive bandstop filters are essential components for these systems to suppress the out-of-band interference signals and protect the adaptive RF transceivers against the reflected waves at the notch frequency [1].

Various absorptive bandstop filters have been reported in previous literatures [2], [3], [4], [5], [6], [7], [8], [9], [10], [11], [12], [13], [14], [15], [16], [17], [18]. Although the filters introduced in [2] and [3] have reflectionless performance at one or two ports, designs for lumped-element filters at low frequencies were introduced. In [4] and [5], absorptive filters with high attenuation characteristics were obtained using low-quality factor (Q) resonators. However, it was difficult to implement distributed filters based on these design theories.

Various design approaches for distributed absorptive filters have been presented in [6], [7], [8], [9], [10], [11], [12], [13], [14] and [15]. The filters in [6] and [7] were designed based on the coupling matrices and routing diagrams at the input port. Design methods using a complementary matching circuit with a single resonator for static and frequency-tunable distributed-element input-reflectionless filters have been reported in [8] and [9]. However, the filters presented in [6], [7], [8] and [9] require auxiliary impedance matching circuits to achieve absorptive responses. The good reflectionless bandstop filters in [10] and [11] were achieved based on coupling diagrams. However, when a tunable filter was implemented using these methods, a low-attenuation characteristic was derived. The filter order of the absorptive bandstop filter proposed in [12] increases with an increase in the number of elements in the filtering and matching circuits. The filter structures reported in [13] and [14] were

The associate editor coordinating the review of this manuscript and approving it for publication was Chun-Hsing Li.

accomplished by transforming the lumped-element filter topology introduced in [2] into the distributed-element filter structures. Additionally, a design method for a distributed element reflectionless bandstop filter was presented using a broadband impedance matching circuit in [15]. However, it is difficult to realize tunable filters based on the filter topologies in [13], [14] and [15].

In this paper, the 4-pole tunable absorptive distributed bandstop filters are designed using folded coupled-lines with an inductor. The proposed design has the following benefits in comparison with the conventional design methods. First, a coupling diagram with a single 45° electrical-length transmission-line source/load coupling could achieve the fourth-order distributed absorptive bandstop filters. In the conventional four-pole absorptive filter coupling diagrams, two quarter-wavelength transmission line coupling structures were used, so that a filter size becomes larger, and the insertion loss increases [1]. However, the proposed filter coupling diagram relatively reduces the filter size, and its insertion loss characteristic is enhanced. The proposed coupling diagram is established based on a four-pole filter transfer function. The 45° electrical-length source/load transmission line coupling structure is realized using a capacitor-loaded transmission line. Second, a distributed tunable absorptive bandstop filter with both the high attenuation characteristic and low return loss response is obtained using the proposed folded coupled-line. When the center frequency of the tunable absorptive bandstop filters is tuned, the attenuation or return loss characteristic at the center frequency is degraded due to the non-controlled resonator Q and coupling coefficient across frequencies. However, the desired coupling coefficients and resonator Qs are satisfied with adjusting asymmetrical capacitors loading the resonators and folding the open-circuited part of the coupled-line. Third, auxiliary impedance-matching circuits are not used to obtain the absorption of the reflected signal. The proposed filter design is achieved by adjusting the coupling coefficients and resonator Qs in a same way as the conventional distributed filter designs. As a result, the distributed absorptive bandstop filters are easily realized. Additionally, the required resonator Qs for the absorptive responses are achieved using finite Q varactors without any additional resistors.

The proposed method was demonstrated by designing two different filters. Filter A is designed with a tuning range of 0.83–1.09 GHz, and Filter B has a center frequency tunability of 1.16–1.47 GHz

II. FILTER DESIGN

A. 4-POLE ABSORPTIVE BANDSTOP FILTER TRANSFER FUNCTION

The transfer functions of a fourth-order bandstop filter are formulated in (1) and (2), as shown in [16]:

$$S_{21} = \frac{p\left(n_4p^3 + n_3p^2 + d_2p + d_1\right)}{p^4 + d_3p^3 + d_2p^2 + d_1p + d_0} \tag{1}$$

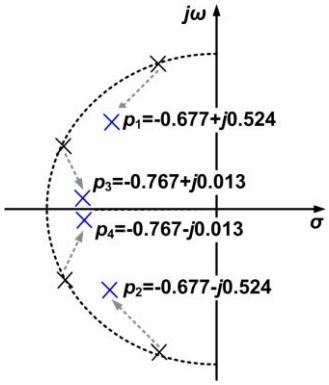

FIGURE 1. Pole locations for the 4-pole absorptive bandstop filter transfer function.

TABLE 1. Coefficients of transfer functions.

Polynomial coefficients
$d_3 = 2.8896$, $d_2 = 3.4020$, $d_1 = 1.9238$, $d_0 = 0.4320$
$n_3 = 2.1196$, $n_2 = 1.7682$, $n_1 = 0.5605$
$m_2 = 0.0641$, $m_1 = 0.0868$, $m_0 = 0$

and

$$S_{11} = \frac{p\left(m_2p + m_1\right) + m_0}{p^4 + d_3p^3 + d_2p^2 + d_1p + d_0}. \tag{2}$$

When the four poles are located at $-0.767 \pm j0.524$ and $-0.677 \pm j0.013$, as shown in Fig. 1, the polynomial coefficients for the S_{11} and S_{21} transfer functions in (1) and (2) are extracted as shown in Table 1 [16]. Note that m_0 of S_{11} becomes zero, and the reflected signal is eliminated at $\omega = 0$ (center frequency), resulting in a perfect absorptive bandstop response. The transfer functions in (1) and (2) can be synthesized using the conventional ladder network method shown in Fig. 2 (a), and the corresponding filter parameters are listed in Table 2 [16]. The entire resonator has a resistor to absorb the reflected signal at the notch frequency. The four resonators are coupled using J-inverters (J_{12}, J_{23}, and J_{34}), and J_{14} is implemented for the cross coupling between the first (C_1 and G_1) and fourth (C_4 and G_4) resonators. Since J_{T12} for the source-load coupling is utilized to achieve the bandstop filter characteristic, a single coupling structure between the input and output ports is required.

The frequency responses of the bandstop filter are displayed in Fig. 2 (b), where the bandstop characteristic (S_{21}) and reflectionless response (S_{11}) can be observed. The proposed 4-pole tunable absorptive bandstop filters are designed based on the structure shown in Fig. 2 (a).

B. FOLDED COUPLED-LINES WITH AN INDUCTOR

Folded coupled-lines with an inductor are implemented using a microstrip-line resonator, as shown in Fig. 3 (a). The open-ended transmission line with admittances Y_{11S} and Y_{12S} is folded to control the coupling coefficient of the coupled-line.

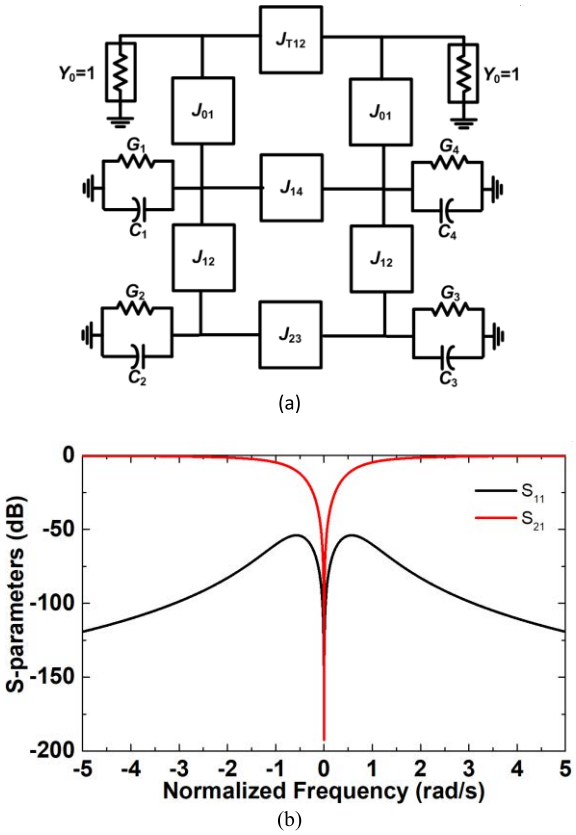

FIGURE 2. (a) Bandstop filter network resulting from (1) and (2) and (b) its frequency responses.

Two series capacitor-resistor circuits with asymmetrical values are loaded to the resonator. The resonator Q is calculated using $Q = \omega_0 C_T/G_T$ as in [17], where C_T and $G_T$are as formulated in (3) and (4).

$$G_T = G_{T12} + \frac{Y_{11}^2 G_{T11}\left(1+(\tan\theta_T)^2\right)}{(Y_{11}-\omega C_{T11}\tan\theta_T)^2 + G_{T11}^2(\tan\theta_T)^2}. \tag{3}$$

$$\begin{aligned} C_T = {} & \frac{\omega C_{T12}}{2\Delta\omega} \\ & + Y_{11}\frac{Y_{11}^2\tan\theta_T - \omega C_{T11}Y_{11}(\tan\theta_T)^2}{2\Delta\omega\left((Y_{11}-\omega C_{T11}\tan\theta_T)^2 + G_{T11}^2(\tan\theta_T)^2\right)} \\ & + Y_{11}\frac{\omega C_{T11}Y_{11} - G_{T11}^2\tan\theta_T - \omega^2 C_{T11}^2\tan\theta_T}{2\Delta\omega\left((Y_{11}-\omega C_{T11}\tan\theta_T)^2 + G_{T11}^2(\tan\theta_T)^2\right)}. \end{aligned} \tag{4}$$

The parameters in (3) and (4) are set as follows: $Y_{11} = Y_{11S} = Y_{12} = Y_{12S} = Y_{14} = 0.02$ S, $\theta_{11S} = 8°$, $\theta_{11} = 22°$, $\theta_{12S} = 9°$, $\theta_{12} = 20°$ at 0.9 GHz. The resonator Q is controlled using the capacitors (C_{11} and C_{12}) and resisters (R_{11} and R_{12}). When $f_0 = 0.9$ GHz and the fractional bandwidth = 0.01 are set based on the parameters in Fig. 2 (b), the required resonator Q is 89.5. Fig. 3 (b) illustrates the calculated Q-factor based on (3) and (4). The Q-factor of 89.5 is satisfied when $R_{11} = 1.6\ \Omega$ and $R_{12} = 0.8\ \Omega$.

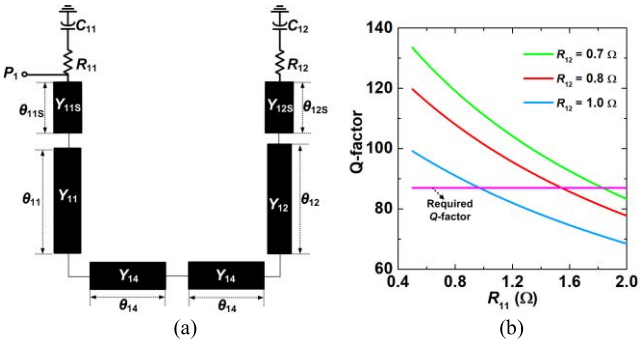

FIGURE 3. (a) Microstrip-line resonator loaded with asymmetrical series capacitor-resistor circuits and (b) its calculated quality factor.

The two resonators in Fig. 3 (a) are coupled with an inductor to implement the circuit shown in Fig. 4 (a), as shown in Fig. 4 (b). The open-ended transmission line with electrical lengths θ_{11S} and θ_{12S} is folded to obtain the required coupling coefficient. J_{T12} in Fig. 2 (a) is typically achieved using a quarter-wavelength transmission line J-inverter to obtain the bandstop response, so that J_{T12} has a magnetic coupling characteristic. Since J_{12}, J_{23}, and J_{14} in Fig. 2 (a) have the same sign as J_{T12}, the J-inverters of J_{12}, J_{23}, and J_{14} should be designed as a magnetic coupling. In Fig. 4 (b), the open-ended transmission line with electrical lengths θ_{11S} and θ_{12S} has the lowest current density on the distributed resonator. Therefore, when an open-ended transmission line with electrical lengths θ_{11S} and θ_{12S} is folded, the parts of the transmission line with the strongest current density could be coupled to easily achieve the magnetic coupling. However, it is difficult to obtain the strong magnetic coupling, since the coupling length of the folded coupled-line decreases. Therefore, the inductor L_{12} is implemented to compensate the weak magnetic coupling of the coupled-line.

The coupling coefficient of the coupled line in Fig. 4 (b) is extracted as suggested in [18].

$$Y_{T12} = -\frac{-Y_{11}^2 Y_{d12}\csc^2\theta_T}{(Y_{d12}+jY_{11}\cot\theta_T - Y_{d11})(Y_{d12}-jY_{11}\cot\theta_T + Y_{d11})} \tag{5}$$

and

$$\begin{aligned} Y_{T11} = {} & j\omega C_{11} - jY_{11}\cot\theta_T \\ & - \frac{Y_{11}^2\csc^2\theta_T\,(-jY_{11}\cot\theta_T + Y_{d11})}{(Y_{d12}+jY_{11}\cot\theta_T - Y_{d11})(Y_{d12}-jY_{11}\cot\theta_T + Y_{d11})}, \end{aligned} \tag{6}$$

where Y_{d12}, Y_{d11}, Y_{in3}, and θ_T are defined in (7)–(10).

$$\begin{aligned} Y_{d12} = {} & -\frac{j}{2}(Y_{o12} - Y_{e12})\cot\theta_{12} \\ & - \frac{j}{2}\left(\frac{Y_{e12}^2\csc^2\theta_{12}}{(jY_{in1}+Y_{e12}\cot\theta_{12})} - \frac{Y_{o12}^2\csc^2\theta_{12}}{jY_{in1}+Y_{o12}\cot\theta_{12}}\right) \\ & - \frac{1}{j\omega L_{12}}, \end{aligned} \tag{7}$$

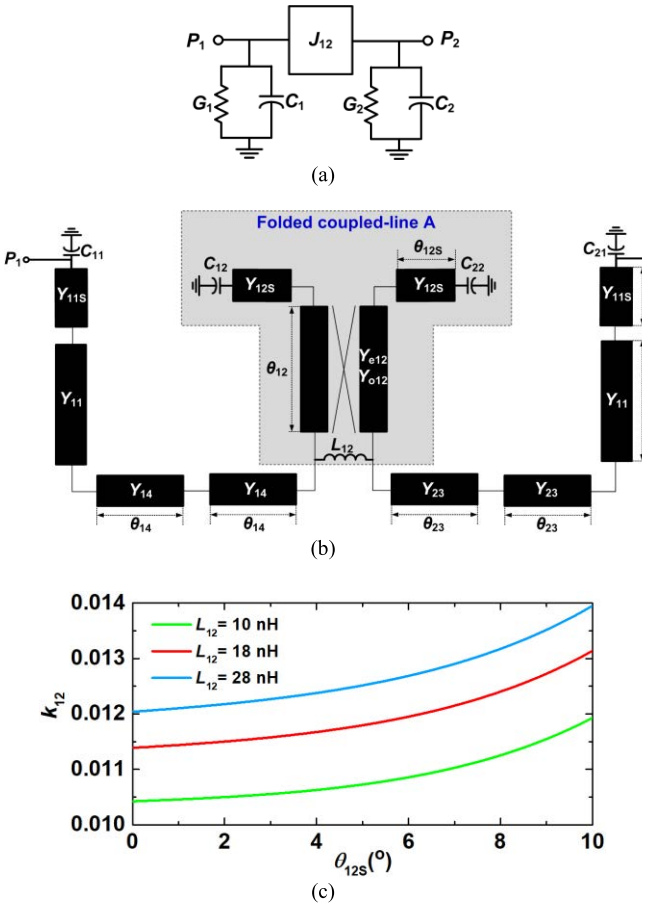

FIGURE 4. (a) Circuit with J_{12} and two resonators in Fig. 2 (a), (b) the resonator pairs with folded coupled-line A, and (c) its calculated coupling coefficient.

$$Y_{d11} = -\frac{j}{2}(Y_{o12} + Y_{e12})\cot\theta_{12} + \frac{j}{2}\left(\frac{Y_{e12}^2\csc^2\theta_{12}}{(jY_{in1}+Y_{e12}\cot\theta_{12})} + \frac{Y_{o12}^2\csc^2\theta_{12}}{jY_{in1}+Y_{o12}\cot\theta_{12}}\right) + \frac{1}{j\omega L_{12}}, \quad (8)$$

$$Y_{\text{in3}} = Y_{12S}\frac{j\omega C_{12} + jY_{12S}tan\theta_{12S}}{Y_{12S} - \omega C_{12}tan\theta_{12S}}, \quad (9)$$

and

$$\theta_{\text{T}} = \theta_{11} + \theta_{11\text{S}} + 2\theta_{14} = \theta_{11} + \theta_{11\text{S}} + 2\theta_{23}. \quad (10)$$

Fig. 4 (c) illustrates the calculated coupling coefficient (k_{12}) with parameters as follows: Z_{11} (= $1/Y_{11}$) = $Z_{11\text{S}}$ (= $1/Y_{11\text{S}}$) = 50 Ω, Z_{12} (= $1/Y_{12}$) = 50 Ω, $Z_{\text{e}14}$ (= $1/Y_{\text{e}14}$) = 52 Ω, $Z_{\text{o}14}$ (= $1/Y_{\text{o}14}$) = 48 Ω, $Z_{\text{e}23}$ (= $1/Y_{\text{e}23}$) = 54.5 Ω, $Z_{\text{o}23}$ (= $1/Y_{\text{o}23}$) = 49 Ω, $Z_{\text{e}12}$ (= $1/Y_{\text{e}12}$) = 53 Ω, $Z_{\text{o}12}$(= $1/Y_{\text{o}12}$) = 48 Ω, $C_{11} = C_{21}$ = 3.8 pF, $C_{12} = C_{22}$ = 5.6 pF, $\theta_{11}+\theta_{11\text{S}} = 30°$, $\theta_{14} = 20°$, $\theta_{12} = 20°$, and $\theta_{23} = 20°$ at 0.9 GHz. It can be observed that k_{12} increases with θ_{12}. Moreover, a higher L_{12} resulted in an increased k_{12}. As $\theta_{12\text{S}}$ decreases, the electric and magnetic couplings cancel each other, decreasing the coupling value. Therefore, the magnetic coupling was obtained by folding the open-ended part.

The circuit with J_{14} in Fig. 5 (a) is designed as a resonator pair with a folded coupled-line B, as shown in Fig. 5 (b). The open-ended transmission line with an electrical length of $\theta_{12} + \theta_{12\text{S}}$ was also folded to obtain the magnetic coupling. The coupling coefficient of the coupled-line in Fig. 5 (b) is extracted as in [18] (11), as shown at the bottom of the next page. and (12), as shown at the bottom of the next page, where Y_{C12}, Y_{C11}, Y_{in3} and $\theta_{\text{T}12}$ are calculated in (13)–(16).

$$Y_{C12} = -\frac{j}{2}(Y_{o14} - Y_{e14})\cot\theta_{14} - \frac{j}{2}\left(\frac{Y_{e14}^2\csc^2\theta_{14}}{2Y_{e14}\cot\theta_{14} - \frac{Y_{e14}^2\csc^2\theta_{14}}{jY_{in3}+Y_{e14}\cot\theta_{14}} + \frac{2}{\omega L_{14}}} - \frac{Y_{o12}^2\csc^2\theta_{14}}{2Y_{o14}\cot\theta_{14} - \frac{Y_{o14}^2\csc^2\theta_{14}}{jY_{in3}+Y_{o12}\cot\theta_{14}}}\right), \quad (13)$$

$$Y_{C11} = -\frac{j}{2}(Y_{o14} + Y_{e14})\cot\theta_{14} + \frac{j}{2}\frac{Y_{e14}^2\csc^2\theta_{14}}{2Y_{e14}\cot\theta_{14} - \frac{Y_{e14}^2\csc^2\theta_{14}}{jY_{in3}+Y_{e14}\cot\theta_{14}} + \frac{2}{\omega L_{14}}} + \frac{j}{2}\frac{Y_{o12}^2\csc^2\theta_{14}}{2Y_{o14}\cot\theta_{14} - \frac{Y_{o14}^2\csc^2\theta_{14}}{jY_{in3}+Y_{o14}\cot\theta_{14}}}, \quad (14)$$

$$Y_{\text{in3}} = Y_{12}\frac{j\omega C_{12} + jY_{12}tan\theta_{T12}}{Y_{12} - \omega C_{12}tan\theta_{T12}}, \quad (15)$$

and

$$\theta_{\text{T}12} = \theta_{11} + \theta_{11\text{S}} + 2\theta_{14} = \theta_{11} + \theta_{11\text{S}} + 2\theta_{23}. \quad (16)$$

Fig. 5 (c) shows the calculated coupling coefficient (k_{14}) using (11) and (12) with the same parameters as in Fig. 4 (c). The required magnetic coupling coefficient is also accomplished based on the structure in Fig. 5 (b). It can be observed that k_{14} increases with $\theta_{12\text{S}}$, and a higher L_{14} resulted in an increased k_{14}.

In the bandstop filters, $J_{\text{T}12}$ in Fig. 2 (a) is typically realized as a quarter-wavelength transmission line. When a capacitor-type J-inverter (C_{01}) is employed as J_{01}, an additional capacitor for $J_{\text{T}12}$ is required to absorb the C_{01} of J_{01}. In addition, the electrical length between the input and output ports is reduced to 45°. Therefore, a capacitor-loaded transmission line was employed, as shown in Fig. 6. The design equations are extracted based on the ABCD parameters of the two transmission-line inverters as follows:

$$\omega C_{T12} = 1/Z_{T12}, \quad (17)$$

$$Z_{T12} = \sqrt{2}\,Z_{12}, \quad (18)$$

$$cos\theta_{T12} = 1/\sqrt{2}. \quad (19)$$

As a result, the electrical length of $\theta_{\text{T}12}$ becomes 45° based on (19).

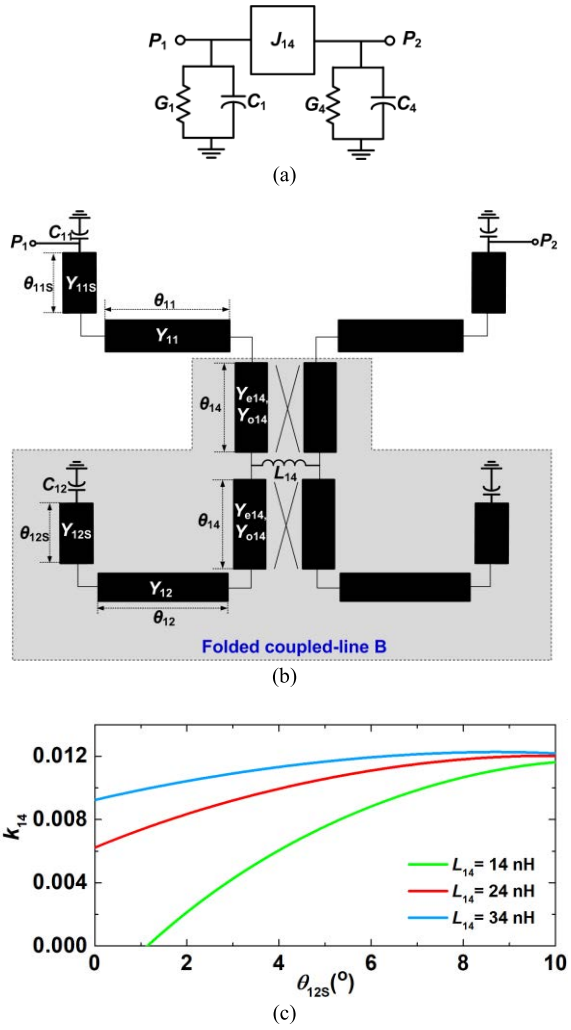

FIGURE 5. (a) Circuit with J_{14} and the two resonators in Fig. 2 (a), (b) the resonator pairs with folded coupled-line B, and (c) its calculated coupling coefficient.

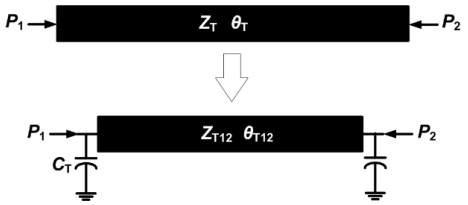

FIGURE 6. Quarter-wavelength transmission line and a capacitor-loaded transmission line.

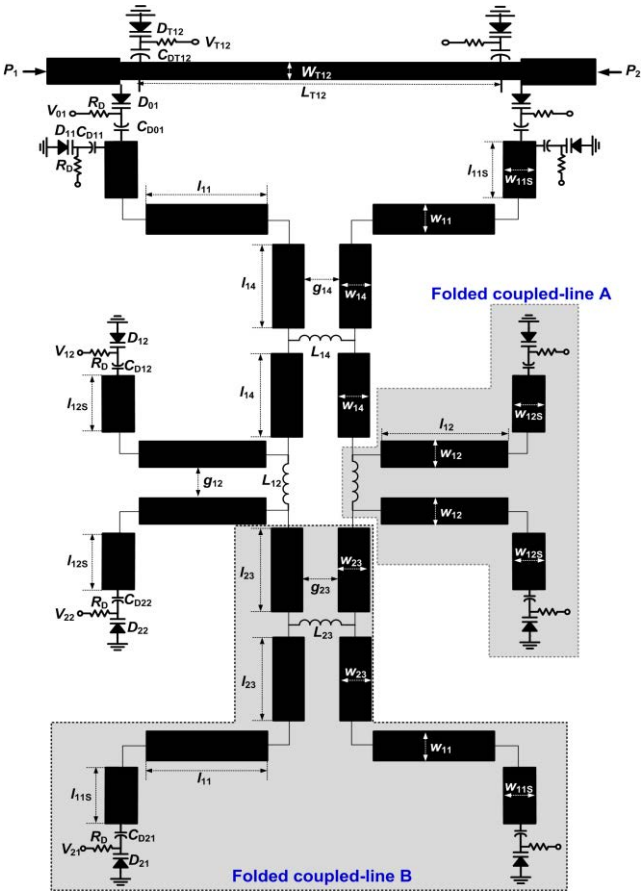

FIGURE 7. Proposed filter configuration.

C. TUNABLE FILTER DESIGN

As shown in Fig. 7, the proposed tunable absorptive bandstop filter is designed using the folded coupled lines A and B shown in Fig. 4 and 5, respectively. J_{T12} was obtained using the transmission line loaded with two capacitors, as shown in Fig. 6. A capacitor-type J-inverter (C_{D01} and D_{01}) is used for input/output coupling.

The two filters were designed based on the proposed filter structure shown in Fig. 7, and a detailed design procedure for Filter A is shown in the next. Although the design procedure for another filter is omitted for brevity, it is essentially identical to that used to design Filter A.

Firstly, the coupling coefficients and the resonator Qs are calculated. Filter A is designed at $f_0 = 0.9$ GHz with

$$Y_{T11} = j\omega C_{11} - jY_{11}\cot\theta_{T11} - \frac{Y_{11}^2\csc^2\theta_{T11}\left(-jY_{11}\cot\theta_{T11} + Y_{C11}\right)}{\left(Y_{C12} + jY_{11}\cot\theta_{T11} - Y_{C11}\right)\left(Y_{C12} - jY_{11}\cot\theta_{11} + Y_{C11}\right)} \tag{11}$$

$$Y_{T12} = -\frac{-Y_{11}^2 Y_{C12}\csc^2\theta_{T11}}{\left(Y_{C12} + jY_{11}\cot\theta_{T11} - Y_{C11}\right)\left(Y_{C12} - jY_{11}\cot\theta_{T11} + Y_{C11}\right)} \tag{12}$$

TABLE 2. Parameters of a Filter in fig. 2 (A).

Filter parameters
J_{01} = 1.404, J_{12} = 0.109, J_{23} = 1, J_{14} = 0.99, $G_1 = G_4$ = 0.98 , $C_1 = C_4$ = 2.56 F, $G_2 = G_3$ = 1.3025, $C_2 = C_3$ = 1.924

a fractional bandwidth of 0.03. The coupling coefficients (k_{12}, k_{23}, and k_{14}) are 0.013, 0.016, and 0.012, respectively, based on the parameters listed in Table 2. Moreover, the Q for the resonator with varactors D_{11} and D_{12} is required to be 87.5, whereas that for the resonator including varactors D_{21} and D_{22}, is 49.2 based on Table 2.

Secondly, the capacitor-loaded resonator is designed considering the required resonator Q (=87.5) as shown in Fig. 3. Initially, the admittances are determined as $Y_{11} = Y_{11S} = Y_{14} = Y_{12S}$ in Fig. 3 to achieve the required resonant frequency, easily. When the coupling coefficients are adjusted, the variation of Y_{14} and Y_{12} is minimized due to the control of the gaps and the inductors between resonators. When $Y_{11} = Y_{11S} = Y_{12} = Y_{12S} = Y_{14} = 0.02$ S and $\theta_{11S}+\theta_{11}+\theta_{12S}+\theta_{12}+\theta_{14} = 100°$ at 0.9 GHz, $C_{11} = 3.6$ pF, and $C_{12} = 7.7$pF, $R_{11} = 1.6\ \Omega$ and $R_{12} = 0.8\ \Omega$ are extracted based on (3) and (4) as shown in Fig. 3(b).

Next, the parameters of the folded coupled-lines in Fig. 4(b) and 5(b) are extracted to satisfy the required coupling coefficients. The coupling coefficients (k_{12}, k_{23}, and k_{14}) for the coupled-lines are calculated based on (5)-(6) and (11)-(12). The initial values for the coupled-lines are used as $Y_{11} = Y_{11S} = Y_{12} = Y_{12S} = Y_{14} = 0.02$ S and $\theta_{11S} + \theta_{11} + \theta_{12S} + \theta_{12} + \theta_{14} = 100°$ for the resonators. The final values for the coupled-lines are determined by changing the folded electrical lengths (θ_{11S}andθ_{12S}) and inductors (L_{12}, L_{14}, and L_{34}) as shown in Fig. 4(c) and 5(c). The design parameters are shown in Table 3 to obtain the required coupling coefficients. High-Q air-coil inductors (080xSQ, $L_{12} = L_{23} = 18$ nH, $L_{14} = 24$ nH, and $Q = 140$ at 900 MHz) are used. The even- and odd-mode impedances are similar to $Z_{11}(= 1/Y_{11} = 50\ \Omega)$ due to the control of the gap and inductors between the resonators. Therefore, the resonator Q and resonant frequency are not significantly changed. The simulation for the coupled-lines in Fig. 4(b) and 5(b) is conducted using Agilent Advanced Design System (ADS) to confirm the coupling coefficients and resonant frequency [19]. The capacitor-loaded transmission line is designed as shown in Fig. 6. $Z_{T12} = 70.7\ \Omega$ and $\theta_{T12} = 45°$ are extracted using (17)-(19).

The varactors are selected to yield the desired tuning range and resonator Q. As shown in Fig. 8, when $Y_{11} = 0.02$ S and filter tuning range = 35 % are selected, the capacitance ratio (C_{Ratio}) is 2.35 [20]. An SMV1413 varactor (C = 9.24–1.77 pF, Capacitance ratio = 5.2, Q = 94.6 @ 1GHz, bias voltages=0-30 V, $R_S = 0.35\ \Omega$) is selected as D_{11} and D_{21} to obtain the required capacitances. Two SMV1413 diodes were connected in parallel for D_{12} and D_{21} to decrease

TABLE 3. Parameters of a Filter A in fig. 9.

Filter parameters
$Z_{11}(= 1/Y_{11}) = Z_{11S}(= 1/Y_{11S}) = 50\ \Omega$, $Z_{12}(= 1/Y_{12}) = 50\ \Omega$, $Z_{e14}(= 1/Y_{e14}) = 52\ \Omega$, $Z_{o14}(= 1/Y_{o14}) = 48\ \Omega$, $Z_{e23}(= 1/Y_{e23}) = 54.5\ \Omega$, $Z_{o23}\ (= 1/Y_{o23}) = 49\ \Omega$, $Z_{e12}\ (= 1/Y_{e12}) = 53\ \Omega$, $Z_{o12}\ (= 1/Y_{o12}) = 48\ \Omega$, $Z_{T12} = 70.7\ \Omega$, $C_{11} = C_{21} = 3.8$ pF, $C_{12} = C_{22} = 5.6$ pF, $\theta_{11} + \theta_{11S} = 30°$, $\theta_{14} = 20°$, $\theta_{12} = 20°$, $\theta_{T12} = 45°$, $\theta_{23} = 20°$ at 0.9 GHz.

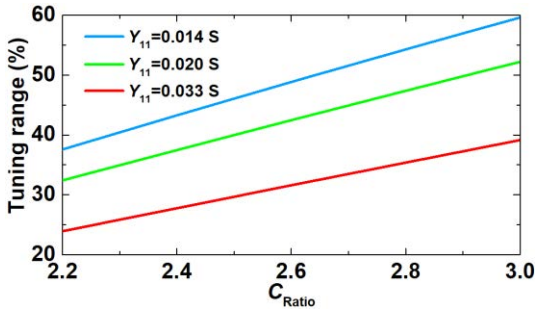

FIGURE 8. Filter tuning range vs. capacitance ratio (C_{Ratio}).

the varactor resistance and increase the varactor capacitance. The varactor Q and C_{Ratio} of SMV1413 are higher than the calculated requirements (Q = 87.5 and C_{Ratio} = 2.35). However, the required Q and C_{Ratio} are finally obtained due to the microstrip line Q and DC-blocking capacitors for varactors. Filter A is fabricated on a 30 mil Duroid substrate ($\varepsilon_r = 3.48$, Rogers RT/Duroid 4350). ATC600L chip capacitors ($R_S = 0.12\ \Omega$, $C_{D11} = 12$ pF, $C_{D12} = C_{D21} = 13.6$ pF (= two 6.8 pF capacitors), $C_{D22} = 25$ pF, $C_{D01} = 4.7$ pF, $C_{DT12} = 4.7$ pF, and $Q = 100$ at 1 GHz) are used as DC blocking capacitors. When the resonator is simulated with a simplified model of the varactors in the Agilent Advanced Design System (ADS), the resonator Qs of 87.5 and 49.2 were obtained with selecting the capacitance of DC blocking capacitors.

Finally, the tunable absorptive bandstop filter is realized as shown in Fig. 7. The folded coupled-line A and B are arranged to realize k_{12}, k_{23}, and k_{14}. The capacitor-loaded transmission line for k_{T12} is utilized. An SMV1232 varactor (C = 4.15–0.75 pF, Capacitance ratio = 4.15, Q = 60.9 @ 1GHz, bias voltages=0-15 V, $R_S = 1.5\ \Omega$) is used for D_{01} and D_{T12} to obtain J_{01} [20]. DC biasing is implemented using a 10 kΩ resistor (R_D) to reduce the RF signal leakage through the bias network. Full-wave results are obtained by simulating the filter with a simplified model of the varactors in the Agilent Advanced Design System (ADS). The filter dimensions are obtained based on the distributed filter parameters in Table 3 as follows: $g_{12} = 1.82$ mm, $g_{14} = 2.15$ mm, $g_{23} = 1.93$ mm, $L_{11} = 9.445$ mm, $W_{11} = 1.66$ mm, $L_{11S} = 6$ mm, $W_{11S} = 1.66$ mm, $L_{14} = 4.945$ mm, $W_{14} = 1.66$ mm, $L_{12} = 9.89$ mm, $W_{12} = 1.63$ mm, $L_{23} = 9.9$ mm, $W_{23} = 1.57$ mm, $W_{T12} = 0.9$ mm, and $L_{T12} = 22.7$ mm.

TABLE 4. Parameters of a filter B in fig. 11.

Filter parameters
$Z_{11}(=1/Y_{11}) = Z_{11S}(=1/Y_{11S}) = 50\ \Omega$, $Z_{12}(=1/Y_{12}) = 50\ \Omega$, $Z_{e14}(=1/Y_{e14}) = 53\ \Omega$, $Z_{o14}(=1/Y_{o14}) = 47.5\ \Omega$, $Z_{e23}(=1/Y_{e23}) = 56.5\ \Omega$, $Z_{o23}(=1/Y_{o23}) = 53.5\ \Omega$, $Z_{e12}(=1/Y_{e12}) = 53.5\ \Omega$, $Z_{o12}(=1/Y_{o12}) = 46.5\ \Omega$, $Z_{T12} = 70.7\Omega$, $C_{11} = C_{21} = 3.8$ pF, $C_{12} = C_{22} = 5.6$ pF, $\theta_{11} + \theta_{11S} = 30^\circ$, $\theta_{14} = 20^\circ$, $\theta_{12} = 20^\circ$, $\theta_{T12} = 45^\circ$, and $\theta_{23} = 20^\circ$ at 1.3 GHz.

Filter B is designed, similarly as Filter A, at $f_1 = 1.3$ GHz with fractional bandwidth of 0.02. The coupling coefficients k_{12}, k_{23}, and k_{14} are 0.009, 0.010, and 0.008, respectively, based on the parameters listed in Table 2. Moreover, the Q for the resonator with varactors D_{11} and D_{12} is 110.5, whereas that for the resonator including varactors D_{21} and D_{22}, is 73.8. The filter parameters are shown in Table 4. C_{D11}, C_{D12}, C_{D21}, C_{D22}, C_{D01}, and C_{DT12} are 8.2 pF, 12 pF, 4.3 pF, 8.2 pF, 3 pF, and 3 pF, respectively. The varactors are equal to those of Filter A. The filter dimensions are obtained as $g_{12} = 1.36$ mm, $g_{14} = 1.68$ mm, $g_{23} = 2.94$ mm, $L_{11} = 5.84$ mm, $W_{11} = 1.66$ mm, $L_{11S} = 4$ mm, $W_{11S} = 1.66$ mm, $L_{14} = 3.295$ mm, $W_{14} = 1.64$ mm, $L_{12} = 6.59$ mm, $W_{12} = 1.65$ mm, $L_{23} = 6.63$ mm, $W_{23} = 1.42$ mm, $W_{T12} = 0.9$ mm, and $L_{T12} = 15$ mm.

III. MEASURED RESULTS

A. FILTER A

Fig. 9 shows a photograph of the fabricated Filter A and the simulated and measured results. The 4-pole absorptive bandstop filter response is accomplished. The rejection level is measured as 47 dB at 0.89 GHz. The measured return loss is 38 dB at 0.89 GHz, and $S_{11} < -11$ dB is obtained in the frequency range 0.7–1.1 GHz. Also, the measured insertion losses are 0.75 dB at 0.79 GHz and 0.77 dB at 0.99 GHz, respectively. The measurements agreed well with the simulation results. The measured wideband return loss is slightly different from the simulated result owing to the error in the varactor modeling.

The notch frequency of Filter A is tuned as shown in Fig. 10. When the notch frequency is adjusted, the absorptive response and high attenuation characteristics are shown simultaneously. The center frequency tuning range is 0.83–1.09 GHz with rejection levels of 41–48 dB and −10 dB rejection bandwidths of 21–25 MHz. The return loss at the notch frequencies is 16.2–38 dB, and the insertion loss is measured in the range 0.55–0.81 dB at a 100 MHz offset frequency from the center frequency.

B. FILTER B

Another 4-pole tunable absorptive bandstop filter (Filter B) is displayed in Fig. 11 (a), and the measured and simulated absorptive notch responses are shown in Fig. 11 (b). The measured rejection level is 40.1 dB at 1.23 GHz. The insertion loss

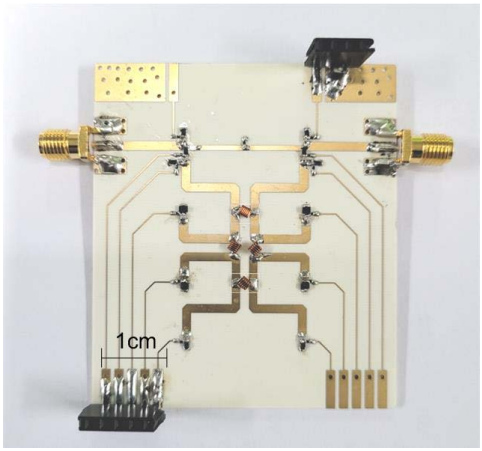

(a)

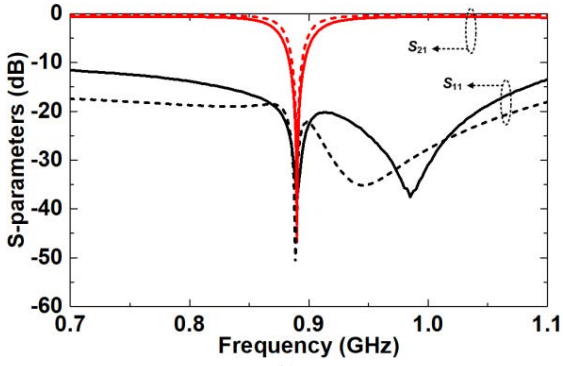

(b)

FIGURE 9. (a) Fabricated Filter A and (b) the measured and simulated responses. (Solid line: measurements; dotted line: simulations.)

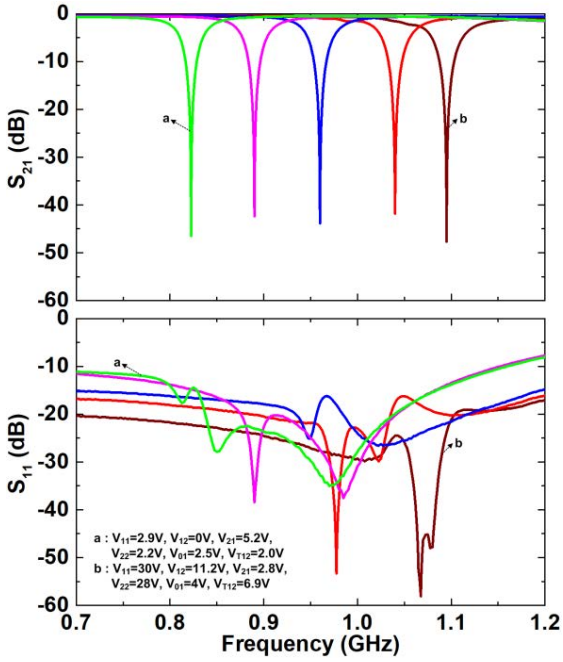

FIGURE 10. Measured frequency responses of the fabricated Filter A.

is 0.81 dB at 1.13 GHz and 0.85 dB at 1.33 GHz, respectively. The notch frequency return loss is 34 dB.

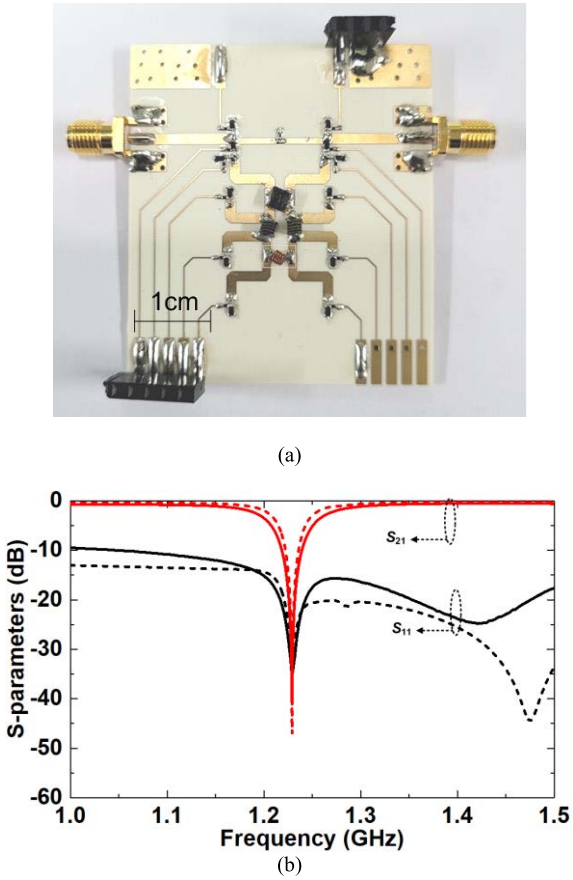

FIGURE 11. (a) Fabricated Filter B and (b) the measured and simulated responses. (Solid line: measurements; dotted line: simulations.)

The center frequency is controlled, as shown in Fig. 12. The notch frequency covers 1.16–1.47 GHz with rejection levels of 40.1–51 dB, and -10 dB rejection bandwidths of 23–26 MHz. The return loss is 14–34 dB at the center frequency, and the insertion loss at a 100 MHz offset frequency from the notch frequency is measured as 0.8–0.89 dB.

C. COMPARISON WITH OTHER FILTERS

Table 5 summarizes the comparison of this study with the existing tunable distributed absorptive bandstop filters in the previous literatures. In [1], a 4-pole tunable absorptive bandstop filter was introduced, whose return loss <5 dB at the notch frequency is shown even though the filter has the rejection level >40 dB. The design methods in [6] and [7] have the complicated filter structure including an auxiliary circuit. Although the tunable absorptive filter in [11] was obtained without the additional impedance-matching network, a low rejection level of 20-28 dB was yielded due to the 2-pole filter structure. Even though the filter suggested in [15] have both the good attenuation and return loss characteristics, it is difficult to realize the tunable filters. The proposed design produces the rejection level >40.1 dB and the return loss >14 dB based on the 4-pole filter configuration without any auxiliary impedance matching network.

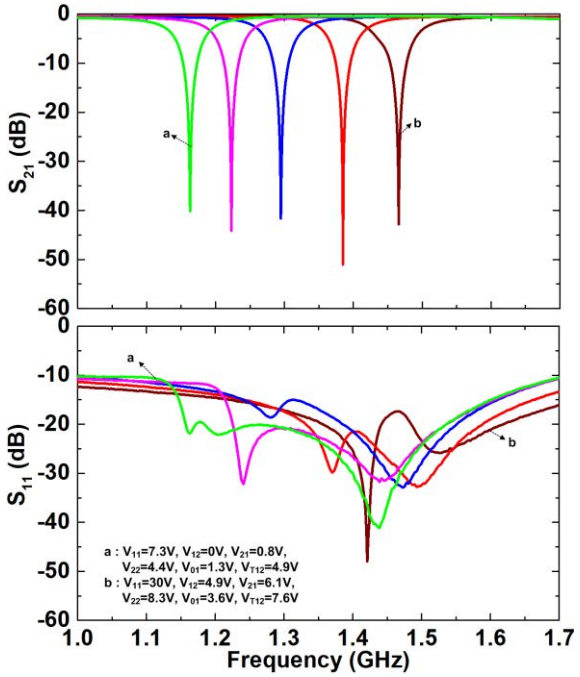

FIGURE 12. Measured frequency responses of the fabricated Filter B.

TABLE 5. Performance comparison with other filters.

	Auxiliary circuit	Filter poles	Tuning range (GHz)	Return loss (dB)	Rejection level (dB)
[1]	No	4	1.8-2.3	5>	40<
[6]	Yes	-	0.18-0.31	22-50	30.7-33.4
[7]	Yes	3	1.93	11.3	36.8
[11]	No	2	2.3-2.5	15<	20-28
[15]	Yes	2	2.0	<15	<40
This study	No	4	0.83-1.09/ 1.16-1.47	16.2-38/ 14-34	41-48/ 40.1-51

IV. CONCLUSION

In this paper, 4-pole tunable absorptive dual-notch filters are proposed. A filter transfer function for 4-pole absorptive bandstop filters was established and folded coupled-lines with a lumped inductor and a finite Q varactor was used to obtain the coupling coefficient based on the filter transfer function. Two filters were designed and tested. In the future, RF MEMS switched capacitors will be used to expect a significant improvement in insertion loss, power handling, and linearity [21].

REFERENCES

[1] M. D. Hickle and D. Peroulis, "Theory and design of frequency-tunable absorptive bandstop filters," *IEEE Trans. Circuits Syst. I, Reg. Papers*, vol. 65, no. 6, pp. 1862–1874, Jun. 2018.

[2] M. A. Morgan, W. M. Groves, and T. A. Boyd, "Reflectionless filter topologies supporting arbitrary low-pass ladder prototypes," *IEEE Trans. Circuits Syst. I, Reg. Papers*, vol. 66, no. 2, pp. 594–604, Feb. 2019.
[3] J. Lee, B. Lee, S. Nam, and J. Lee, "Rigorous design method for symmetric reflectionless filters with arbitrary prescribed transmission response," *IEEE Trans. Microw. Theory Techn.*, vol. 68, no. 6, pp. 2300–2307, Jun. 2020.
[4] J. Lee, T. C. Lee, and W. J. Chappell, "Lumped-element realization of absorptive bandstop filter with anomalously high spectral isolation," *IEEE Trans. Microw. Theory Techn.*, vol. 60, no. 8, pp. 2424–2430, Aug. 2012.
[5] T.-H. Lee, B. Kim, K. Lee, W. J. Chappell, and J. Lee, "Frequency tunable low-Q lumped-element resonator bandstop filter with high attenuation," *IEEE Trans. Microw. Theory Techn.*, vol. 64, no. 11, pp. 3549–3556, Nov. 2016.
[6] D. Psychogiou and R. Gómez-García, "Reflectionless adaptive RF filters: Bandpass, bandstop, and cascade designs," *IEEE Trans. Microw. Theory Techn.*, vol. 65, no. 11, pp. 4593–4605, Nov. 2017.
[7] R. Gomez-Garcia, J.-M. Munoz-Ferreras, and D. Psychogiou, "High-order input-reflectionless bandpass/bandstop filters and multiplexers," *IEEE Trans. Microw. Theory Techn.*, vol. 67, no. 9, pp. 3683–3695, Sep. 2019.
[8] S.-W. Jeong, T.-H. Lee, and J. Lee, "Absorptive filter prototype and distributed-element absorptive bandpass filter," in *IEEE MTT-S Int. Microw. Symp. Dig.*, Aug. 2018, pp. 1–4.
[9] S.-W. Jeong, T.-H. Lee, and J. Lee, "Frequency- and bandwidth-tunable absorptive bandpass filter," *IEEE Trans. Microw. Theory Techn.*, vol. 67, no. 6, pp. 2172–2180, Jun. 2019.
[10] D. R. Jachowski, "Passive enhancement of resonator Q in microwave notch filters," in *IEEE MTT-S Int. Microw. Symp. Dig.*, Jun. 2004, pp. 1315–1318.
[11] D. R. Jachowski, "Compact, frequency-agile, absorptive bandstop filters," in *IEEE MTT-S Int. Microw. Symp. Dig.*, Jun. 2005, pp. 513–516.
[12] R. Gómez-García, J.-M. Muñoz-Ferreras, and D. Psychogiou, "Symmetrical quasi-absorptive RF bandpass filters," *IEEE Trans. Microw. Theory Techn.*, vol. 67, no. 4, pp. 1472–1482, Apr. 2019.
[13] M. A. Morgan and T. A. Boyd, "Reflectionless filter structures," *IEEE Trans. Microw. Theory Techn.*, vol. 63, no. 4, pp. 1263–1271, Apr. 2015.
[14] M. A. Morgan, *Reflectionless Filters*. Norwood, MA, USA: Artech House, 2017.
[15] J. Lee and J. Lee, "Distributed-element reflectionless bandstop filter with a broadband impedance matching," *IEEE Microw. Wireless Compon. Lett.*, vol. 30, no. 6, pp. 561–564, Jun. 2020.
[16] A. C. Guyette, I. C. Hunter, and R. D. Pollard, "The design of microwave bandpass filters using resonators with nonuniform Q," *IEEE Trans. Microw. Theory Techn.*, vol. 54, no. 11, pp. 3914–3922, Nov. 2006.
[17] D. M. Pozar, *Microwave Engineering*. Hoboken, NJ, USA: Wiley, 2012.
[18] M. A. El-Tanani and G. M. Rebeiz, "High-performance 1.5–2.5-GHz RF-MEMS tunable filters for wireless applications," *IEEE Trans. Microw. Theory Techn.*, vol. 58, no. 6, pp. 1629–1637, Jun. 2010.
[19] J.-S. Hong and M. J. Lancaster, *Microstrip Filters for RF/Microwave Applications*, 2nd ed. Hoboken, NJ, USA: Wiley, 2011.
[20] G. Matthael, L. Young, and E. M. T. Jones, *Microwave Filters, Impedance-Matching Networks, and Coupling Structures*. Norwood, MA, USA: Arthech House, 1980.
[21] G. M. Rebeiz, K. Entesari, I. C. Reines, S.-J. Park, M. A. El-Tanani, A. Grichener, and A. R. Brown, "Tuning in to RF MEMS," *IEEE Microw. Mag.*, vol. 10, no. 6, pp. 55–72, Oct. 2009.

YOUNG-HO CHO (Member, IEEE) received the B.Eng. and Ph.D. degrees in electronic engineering from Sogang University, Seoul, South Korea, in 2005 and 2012, respectively. From 2013 to 2014, he was a Postdoctoral Researcher with the Department of Electrical and Computer Engineering, University of California at San Diego (UCSD), La Jolla, CA, USA. From 2015 to 2018, he was a Senior Researcher at the Defense Industry Technology Center (DITC), Agency for Defense Development (ADD), Seoul. He is currently an Assistant Professor with the Electrical and Communication Engineering Department, Daelim University, Anyang, South Korea. His research interests include RF filters, tunable and multi-band circuits, antennas, and RF systems.

CHEOLSOO PARK (Member, IEEE) received the B.Eng. degree in electrical engineering from Sogang University, Seoul, South Korea, the M.Sc. degree from the Biomedical Engineering Department, Seoul National University, Seoul, and the Ph.D. degree in adaptive nonlinear signal processing from the Imperial College London, London, U.K, in 2012. From 2012 to 2013, he was a Postdoctoral Researcher at the University of California San Diego. He is currently an Associate Professor with the Computer Engineering Department, Kwangwoon University, Seoul. His research interests include primarily in the areas of machine learning and adaptive and statistical signal processing, with applications in healthcare, computational neuroscience, and wearable technology.

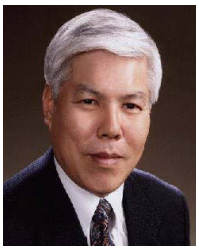

SANG-WON YUN (Life Member, IEEE) received the B.Sc. and M.Sc. degrees in electronic engineering from Seoul National University, Seoul, South Korea, in 1977 and 1979, respectively, and the Ph.D. degree in electrical engineering from The University of Texas at London, Austin, in 1984. Since 1984, he has been a Professor with the Department of Electronic Engineering, Sogang University, Seoul. From January 1988 to December 1988, he was a Visiting Professor with The University of Texas at Austin. From 2009 to 2011, he worked for the Korea Communications Commission (KCC) as a Project Manager. His research interests include microwave and millimeter-wave devices and circuits. He was the Chairperson of the IEEE Microwave Theory and Techniques Society (IEEE MTT-S) Korea Chapter, from 2000 to 2004. He was the President of the Korea Institute of Electromagnetic Engineering and Science (KIEES), in 2008.